construction materials

MDPI

Article

Fresh-State Properties and Machine-Learning Prediction of Sulfoaluminate Cement Grout for Water-Rich Tunnels

Tao Peng [1,2,3], Dongxing Ren [2], Binjia Li [1,2,3], Peng Xue [2], Hongye Liao [1,2] and Yang Li [3,*]

[1] China MCC5 Group Corp. Ltd., Chengdu 610023, China; ptgeo93@outlook.com (T.P.); tunnel123@163.com (B.L.); a13881808803@126.com (H.L.)
[2] Chengdu Surveying Geotechnical Research Institute Co., Ltd. of MCC, Chengdu 610023, China; rendx07@126.com (D.R.); xuep07@126.com (P.X.)
[3] School of Civil Engineering, Southwest Jiaotong University, Chengdu 610031, China
* Correspondence: yangli_civil@swjtu.edu.cn

Abstract

This study investigated sulfoaluminate cement grout intended for water-rich tunnel applications and developed machine-learning models for predicting its fresh-state properties. The experimental programme included a 31-mixture base series varying the water-to-binder ratio, Class F fly ash, steel slag, and polycarboxylate ether (PCE) superplasticizer dosage; a hydroxyethyl cellulose (HEC)-modified series with a fixed binder composition; and a static-water turbidity series used to evaluate particle dispersion resistance. Flowability, setting time, compressive strength, and turbidity were measured. The results showed that the water-to-binder ratio, fly ash, steel slag, PCE, and HEC affected the balance between workability, setting behaviour, strength development, and static-water dispersion resistance. Increasing the HEC dosage from 0.004 to 0.006 reduced turbidity by 84.1–94.7% under static-water conditions, whereas an HEC dosage of 0.007 reduced the 7 and 28 d compressive strengths by 51.5% and 40.7%, respectively. Machine-learning models trained on the 31-mixture HEC-free dataset provided exploratory predictions of flowability and initial and final setting times. Extra Trees, support vector regression, and Extra Trees gave the lowest nested leave-one-out cross-validation (LOOCV) errors for flowability, initial setting time, and final setting time, with R^2 values of 0.819, 0.743, and 0.767, respectively. Shapley Additive Explanations (SHAP) analysis indicated that the water-to-binder ratio dominated flowability prediction, whereas fly ash contributed strongly to setting-time prediction. The results provide complementary experimental and data-driven evidence for comparing sulfoaluminate cement grout formulations within the investigated composition domain.

Keywords: calcium sulfoaluminate cement; cementitious grout; hydroxyethyl cellulose; static-water dispersion resistance; fresh-state properties; machine learning

Check for updates

Received: 21 July 2026
Revised: 11 September 2026
Accepted: 17 September 2026
Published: 19 September 2026

Copyright: © 2026 by the authors. Licensee MDPI, Basel, Switzerland. This article is an open access article distributed under the terms and conditions of the Creative Commons Attribution (CC BY) license.

1. Introduction

Water and mud inrush constitute major geological hazards during tunnel construction in water-rich fractured rock, fault zones, and karst formations. Such events can destabilize the excavation face, induce ground collapse, interrupt construction, and threaten the safety of underground structures [1–3]. Grouting is therefore widely used to fill water-bearing fractures and cavities, reduce formation permeability, and improve the integrity of weakened surrounding rock. In underwater shield tunnelling and karst ground, however, the injected grout is exposed directly to groundwater before hardening [4]. Hydrodynamic shear, buoyancy, and dilution may disperse cement particles, reduce grout retention, and

produce heterogeneous or discontinuous hardened bodies. Grouts intended for these environments must consequently combine pumpability and diffusion capacity with controllable rapid setting, washout resistance, high slurry retention, and sufficient early strength [5].

Conventional Portland-cement suspensions generally cannot satisfy all these requirements without modification. Cement-sodium silicate dual-fluid systems are widely used to achieve rapid gelation, but their setting behaviour can be sensitive to composition and environmental conditions, while insufficient washout resistance may limit their effectiveness under flowing water [5]. Anti-washout admixtures provide an alternative route by increasing the viscosity, water retention, and cohesion of cementitious suspensions [6–9]. Early studies established fluidity, washout loss, residual strength, and slurry retention as useful indicators for evaluating underwater grout [7,8]. Subsequent research demonstrated that cellulose derivatives, gums, polyacrylamide, and hydrogel-based admixtures can improve washout resistance through water sorption, adsorption, particle bridging, and polymer-network formation [10–12]. Nevertheless, increasing cohesion generally reduces flowability, and excessive polymer addition may retard hydration, entrain air, or reduce hardened strength. Rapid-setting anti-washout grout design therefore involves a multi-property balance rather than the maximization of viscosity or setting rate alone.

Sulfoaluminate cement (SAC) offers a promising binder for rapid water-blocking applications because of its rapid hardening, high early strength, and relatively low clinker-production temperature [13–15]. Its early behaviour is primarily associated with rapid ye'elimite hydration and ettringite formation, while the subsequent development of the hydrate assemblage depends on sulfate availability, water content, and supplementary constituents [16]. Recent studies have consequently investigated SAC-based grouts for water-bearing and broken rock strata [17,18]. Sha et al. showed that a rapid-hardening SAC grout could provide favourable diffusion, anti-washout behaviour, early strength, and reinforcement performance when PCE and cellulose ether were used to regulate its fresh properties [17]. Industrial mineral additions provide additional opportunities to tailor SAC-based grouts. Fly ash can influence ettringite formation, particle packing, setting, and strength development [19], whereas finely ground steel slag has been explored as a mineral component of composite grouts for underground engineering [20]. However, mineral replacement may also dilute rapidly reacting clinker phases or introduce particles with different morphology and reactivity. The combined influence of fly ash and steel slag on the fresh-state and setting behaviour of rapid-hardening SAC paste therefore requires systematic investigation.

Chemical admixtures are needed to reconcile the competing requirements of flowability and underwater stability. PCE improves particle dispersion through electrostatic repulsion and steric hindrance, whereas cellulose ethers increase water retention and suspension cohesion [21–26]. The effectiveness of their combination depends on adsorption, compatibility with early hydration products, polymer chemistry, and dosage [25,26]. Studies of SAC-based materials have shown that HEC and related cellulose ethers can alter water distribution, setting behaviour, and early hydration [23,24]. However, increased water retention does not necessarily indicate adequate underwater stability, and the dosage required to reduce particle dispersion may adversely affect flowability or strength. Turbidity provides a direct indication of the release of fine cementitious particles into the surrounding water and can therefore complement conventional flow, setting, and strength measurements [6,7]. Comparatively few studies have evaluated these properties together in an SAC paste containing fly ash, steel slag, PCE, and HEC. In particular, the combined influence of water content and HEC dosage on cementitious-particle dispersion under static-water conditions remains insufficiently quantified. Increasing water content may improve pumpability but may simultaneously reduce paste cohesion and increase particle

release. This limits the formulation of mixtures that can remain pumpable while rapidly developing resistance to underwater dispersion.

The simultaneous variation of binder composition, water content, and chemical admixtures creates a multidimensional mixture-design problem. In addition, cementitious-material properties may be affected not only by nominal mixture proportions but also by material-source and batch variability. For example, Vasconcellos et al. showed that aggregate batch significantly influenced the elastic modulus of concrete and proposed characteristic values 6–11% lower than the corresponding mean values [27]. Conventional trial-and-error testing can identify controlled trends but becomes inefficient when several mixture variables and performance targets are considered concurrently. Machine-learning methods have increasingly been used to predict the properties of concrete, mortar, and cementitious grout from mixture composition [28–33]. Liu et al. combined laboratory testing and machine learning to predict multiple properties of cement-based grouting materials and subsequently identify potential proportions [29]. Other studies have applied data-driven methods to cement-grout proportioning, multi-objective concrete design, and adaptive experimental selection [30–33]. Nevertheless, model performance can be overestimated when hyperparameter selection and performance evaluation use the same cross-validation information [34]. Moreover, point-prediction accuracy alone does not explain how mixture variables influence model outputs or communicate the uncertainty associated with predictions. SHAP provides model-based attribution of predictions to input variables [35], while distribution-free procedures such as Jackknife+ can provide prediction intervals for new observations [36]. These techniques are particularly relevant to small experimental datasets, provided that validation, interpretation, and applicability limits are reported cautiously.

Therefore, this study investigated the effects of the water-to-binder ratio, Class F fly ash, steel slag, PCE, and HEC on the flowability, setting behaviour, compressive strength, and static-water dispersion resistance of SAC paste. This study addresses this gap by examining how mineral additions, water content, and admixtures jointly affect the fresh-state behaviour and static-water dispersion resistance of SAC grout. In addition, a small-dataset machine-learning analysis was used as a complementary tool to predict flowability and setting time for the HEC-free mixtures and to evaluate the uncertainty of these predictions. The experimental component comprised a 31-mixture HEC-free base series, an HEC performance series based on a fixed reference binder, and a water-to-binder-ratio-HEC turbidity matrix. In a complementary data-driven component, the 31-mixture base dataset was used to predict flowability and initial and final setting times. Candidate algorithms were compared through nested cross-validation, out-of-fold SHAP values were used for model interpretation, and Jackknife+ intervals were used to illustrate prediction uncertainty. The machine-learning analysis was restricted to the HEC-free base mixtures, whereas the HEC experiments independently evaluated workability, setting, strength, and static-water dispersion resistance for the reference binder.

2. Materials and Methods

2.1. Materials

The materials used to prepare the cementitious grout pastes included sulfoaluminate cement (SAC), Class F fly ash, steel slag powder, a polycarboxylate-based superplasticizer (PCE), hydroxyethyl cellulose (HEC), and tap water. R-SAC 42.5 sulfoaluminate cement supplied by Jiahua Special Cement Co., Ltd. (Leshan, China) was used as the primary binder. Class F fly ash and 200-mesh steel slag powder were used as supplementary solid constituents and partially replaced the SAC by mass. PCE was used to regulate

the flowability of the fresh paste, while HEC was used as a viscosity-modifying and anti-dispersion admixture. Tap water was used for all mixtures.

2.2. Mixture Proportions and Preparation

The mixture series and test programme are summarized in Table 1, the detailed mixture can be seen in Appendix A. The SAC, Class F fly ash, 200-mesh steel slag powder, and HEC, when used, were dry-mixed according to the designed proportions. Fly ash, steel slag, and HEC dosages were expressed relative to the total binder mass. Tap water and PCE were subsequently added. The pastes were mixed at low speed for 60 s and high speed for 30 s, followed by a 90 s pause for scraping the blade and bowl, and a final 60 s of high-speed mixing.

Table 1. Summary of experimental series and test programme.

Experimental Series	Number	w/b	FA	Steel Slag	PCE (mL)	HEC	Tests
Water-to-binder-ratio series	4	0.40–0.80	0	0	0	0	F, S
Fly-ash series	5	0.5	0.10–0.50	0	0	0	F, S
Steel-slag series	5	0.5	0	0.10–0.50	0	0	F, S
Fly-ash–steel-slag series	10	0.5	0.10–0.40	0.10–0.40	0	0	F, S
PCE series	3	0.5	0.2	0.2	1–3	0	F, S
Combined w/b–binder series	4	0.60, 0.80	0.10, 0.20	0.10, 0.20	0	0	F, S
HEC performance series	8	0.5	0.1	0.1	0	0–0.007	F, S, C
Static-water turbidity series	12	0.40–0.60	0.1	0.1	0	0.003–0.006	T

Note: FA, steel slag, and HEC are expressed as mass fractions of the total binder. F = flowability; S = initial and final setting times; C = 7 and 28 d compressive strengths; T = static-water turbidity.

Three experimental series were prepared. The base series comprised 31 HEC-free mixtures with varying water-to-binder ratio, fly ash, steel slag, and PCE dosage for flowability and setting-time tests. The HEC performance series used a fixed water-to-binder ratio of 0.50 and a binder containing 80% SAC, 10% fly ash, and 10% steel slag; the HEC dosage ranged from 0 to 0.007 for evaluating flowability, setting time, and 7 and 28 d compressive strengths. The turbidity series used the same binder composition with water-to-binder ratios of 0.40–0.60 and HEC dosages of 0.003–0.006. Flowability, setting time, and turbidity were measured using three independently prepared fresh-paste specimens for each mixture. For compressive strength, three prisms were prepared for each mixture and curing age and then fractured into six half-prisms for testing.

Fresh paste was tested immediately or cast into 40 mm × 40 mm × 160 mm moulds and vibrated for 120 +/− 5 s for compressive-strength testing. The specimens were demoulded after 24 h and cured at 20 +/− 1 °C and a relative humidity of at least 90%. Results from repeated tests were reported as mean ± standard deviation.

2.3. Test Methods

2.3.1. Flowability

Fresh-paste flowability was measured according to GB/T 50448-2015 [37]. The moistened truncated-cone mould was filled with paste and lifted vertically to allow free spreading. After spreading ceased, the maximum diameter and its perpendicular diameter were measured, and their arithmetic mean was taken as the flowability value for that test. For each mixture, three independently prepared specimens were tested, and the mean value and

standard deviation of the three flowability results were reported. The test was completed within 6 min after mixing began.

2.3.2. Setting Time

Initial and final setting times were determined using a Vicat apparatus according to GB/T 1346-2024 [38], with water addition defined as time zero. The initial setting was reached when the needle stopped 4 ± 1 mm above the base plate. After the mould was inverted, final setting was reached when the needle penetrated no more than 0.5 mm and the annular attachment no longer left a visible impression. Each endpoint was confirmed by two successive measurements. Three independently prepared specimens were tested for each mixture, and the mean and standard deviation were reported.

2.3.3. Compression Test

At 7 and 28 d, three 40 mm × 40 mm × 160 mm prisms were first fractured into six half-prisms. Each half-prism was compressed through a 40 mm × 40 mm loading area according to GB/T 17671-2021 [39]. Compressive strength was calculated as $f_c = F_{max}/A$, where f_c is the compressive strength, F_{max} is the maximum load at failure, and A is the loaded area. The mean of six measurements was reported. If one value differed from the mean by more than 10%, it was excluded and the remaining five values were averaged. The result was considered invalid if a second value exceeded this limit or if two or more of the original six values exceeded it. Strength results were reported to 0.1 MPa.

2.3.4. Static-Water Turbidity Test

Static-water turbidity was measured to evaluate the release of fine cementitious particles from fresh paste. Approximately 200 mL of freshly mixed paste was loaded into the grout reservoir and pressure-injected into a container holding 4000 mL of quiescent clean water. Turbidity was measured using a meter with a range of 0–400 NTU. Three independently prepared specimens were tested for each combination, and the mean and standard deviation were reported. When all readings exceeded 400 NTU, the result was reported as >400 NTU and treated as right-censored. These observations were excluded from calculations of numerical means, standard deviations, percentage reductions, and conventional analysis of variance. Lower turbidity indicated less suspended-particle release under the specified static-water conditions, rather than complete anti-washout performance.

2.3.5. Statistical Analysis

Results from three independently prepared specimens were expressed as mean ± standard deviation. Quantifiable turbidity measurements obtained at HEC dosages of 0.004–0.006 were analysed using two-way analysis of variance, with water-to-binder ratio and HEC dosage treated as fixed factors. Their interaction was also evaluated, and statistical significance was defined as $p < 0.05$. Results exceeding 400 NTU at an HEC dosage of 0.003 were excluded from the analysis of variance.

3. Results and Discussion

3.1. Flowability

Figure 1 shows the effects of the investigated mixture variables on paste flowability. The plotted values are the means of three independently prepared specimens, and the error bars in Figure 1a–e indicate the corresponding standard deviations. Flowability generally increased with the water-to-binder ratio, fly ash content, and PCE dosage. Steel slag produced a non-monotonic response, whereas high HEC dosages reduced flowability.

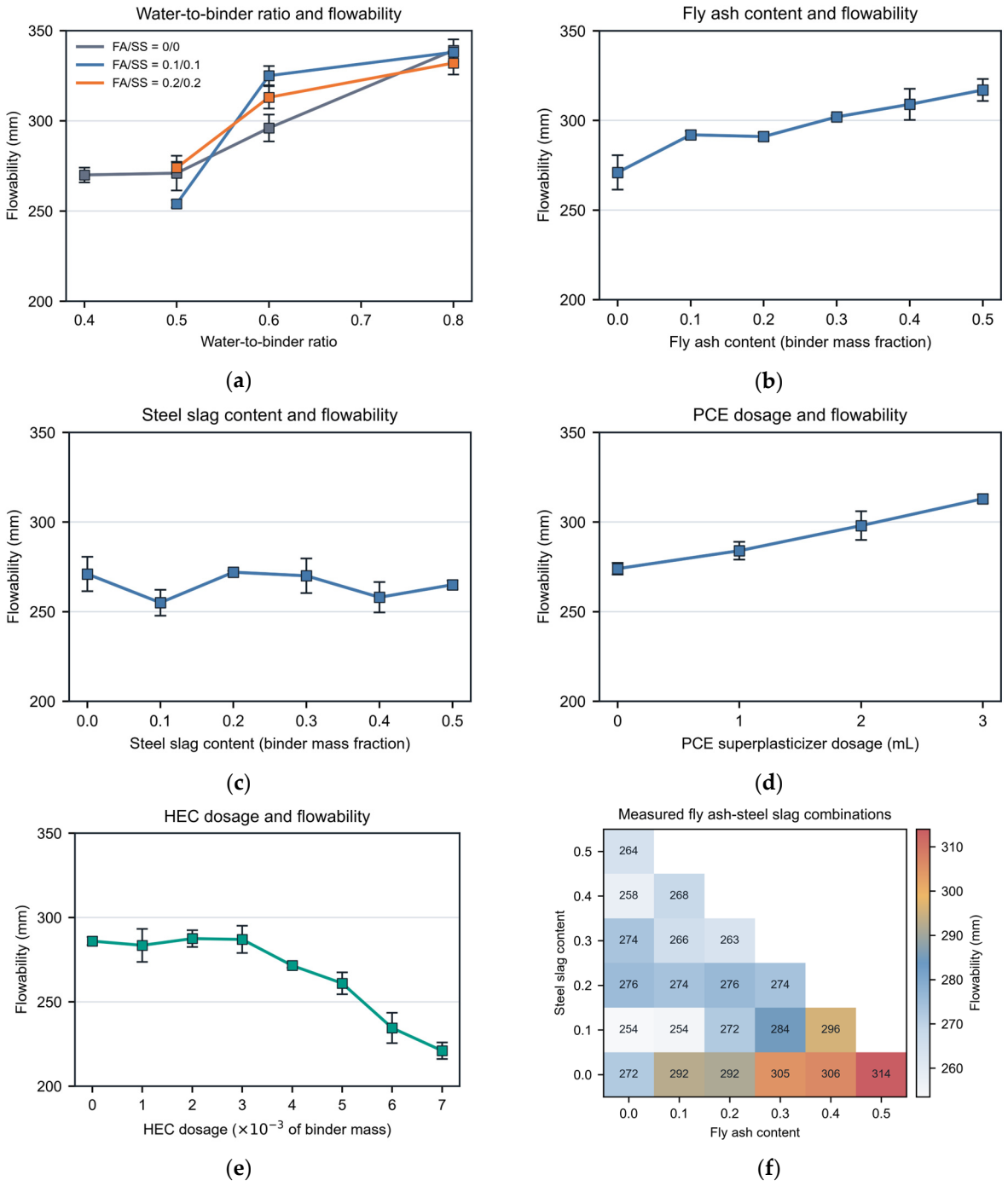


Figure 1. Effects of mixture variables on grout-paste flowability: (**a**) water-to-binder ratio; (**b**) Class F fly ash content; (**c**) steel slag content; (**d**) PCE superplasticizer dosage; (**e**) HEC dosage; (**f**) measured fly-ash-steel-slag combinations. Error bars in panels (**a**–**e**) represent the standard deviation of three independently prepared specimens.

As shown in Figure 1a, the water-to-binder ratio produced the largest overall change. For the paste without fly ash or steel slag, increasing the water-to-binder ratio from 0.40 to 0.80 increased the flowability from 267.5 to 335.5 mm. At a ratio of 0.80, the investigated binder compositions produced similar values of 335.5–336.5 mm, indicating that the influence of binder composition became less evident at high water contents. This behaviour may be attributed to the greater amount of free water available for particle separation and lubrication, thereby reducing flow resistance [40,41].

Increasing the fly ash fraction from 0 to 0.50 increased the flowability from 272.0 to 314.0 mm (Figure 1b). Since particle packing and early hydration were not directly examined, this improvement can be interpreted from both particle-packing and early-hydration perspectives based on previous studies. Class F fly ash commonly contains smooth, approximately spherical particles, which can reduce interparticle friction and facilitate particle rearrangement during spreading through a ball-bearing effect. In addition, replacing part of the rapidly hydrating sulfoaluminate cement with fly ash may modify the early hydration process and reduce early structural build-up during the short flowability test, thereby preserving more free water for lubrication [42,43].

Steel slag produced a less systematic response (Figure 1c). The flowability varied between 253.5 and 275.5 mm as the steel slag fraction increased from 0 to 0.50, without a monotonic trend. Figure 1f further shows that the highest value, 314.0 mm, was obtained at a fly ash fraction of 0.50 without steel slag, whereas relatively low values occurred in mixtures containing 0.10 steel slag and low fly ash fractions. Thus, the effect of steel slag appeared to depend on the accompanying binder composition rather than solely on its replacement fraction. Unlike fly ash, steel slag powder may introduce particles with different surface characteristics, density, and calcium-bearing mineral phases [20]. These characteristics can affect water demand, particle packing, interparticle interactions, and early hydration behaviour in cementitious pastes [44]. Therefore, the non-monotonic flowability response observed here is more reasonably interpreted as the result of coupled physical and early hydration effects among sulfoaluminate cement, fly ash, and steel slag, rather than a simple replacement-level or dilution effect. Composition-dependent interactions between steel slag and calcium sulfoaluminate cement have also been reported [44].

As shown in Figure 1d, increasing the PCE dosage from 0 to 3 mL increased the flow diameter from 276.0 to 313.5 mm. PCE can improve cement-particle dispersion through steric hindrance and release water retained within particle agglomerates, thereby reducing flow resistance. The observed trend agrees with previous studies in which PCE increased the fluidity of calcium sulfoaluminate cement pastes [45,46].

The HEC series was evaluated at a fixed water-to-binder ratio of 0.50 using a binder containing 80% SAC, 10% fly ash, and 10% steel slag. HEC had little effect at dosages up to 0.003, with flowability remaining between 283.5 and 287.5 mm (Figure 1e). At higher dosages, flowability decreased progressively, reaching 221.0 mm at an HEC dosage of 0.007. This reduction may be attributed to the thickening and water-retention effects of cellulose ether, which increase liquid-phase viscosity and restrict particle movement [21]. Excessive HEC should therefore be avoided when adequate grout flowability is required.

3.2. Setting Time

Figure 2 shows the effects of the mixture variables on initial and final setting times. Fly ash, steel slag, and high HEC dosages generally prolonged setting, whereas the effect of the water-to-binder ratio depended on binder composition.

As shown in Figure 2a, the initial setting time of the paste without fly ash or steel slag changed non-monotonically with increasing water-to-binder ratio. It decreased from 15 min at a water-to-binder ratio of 0.40 to 14 min at 0.60 and then increased to 18 min at 0.80. Meanwhile, the final setting time increased from 18 to 24 min. For the paste containing 10% fly ash and 10% steel slag, increasing the water-to-binder ratio from 0.50 to 0.80 extended the initial and final setting times from 25 and 52 min to 46 and 68 min, respectively. Higher water content generally increases particle separation and requires more hydration products to establish a continuous rigid network [47]. Since Vicat setting is determined from penetration resistance, the measured setting time is also affected by the consistency and structural build-up of the fresh paste, not only by the rate of hydration. Mixtures

with higher initial flowability may require a longer time to develop sufficient resistance to needle penetration, whereas mixtures with lower flowability or faster workability loss may reach the apparent setting threshold earlier [41]. The contrasting responses of the unblended and blended pastes suggest that the influence of water content depended on binder composition and consistency evolution.

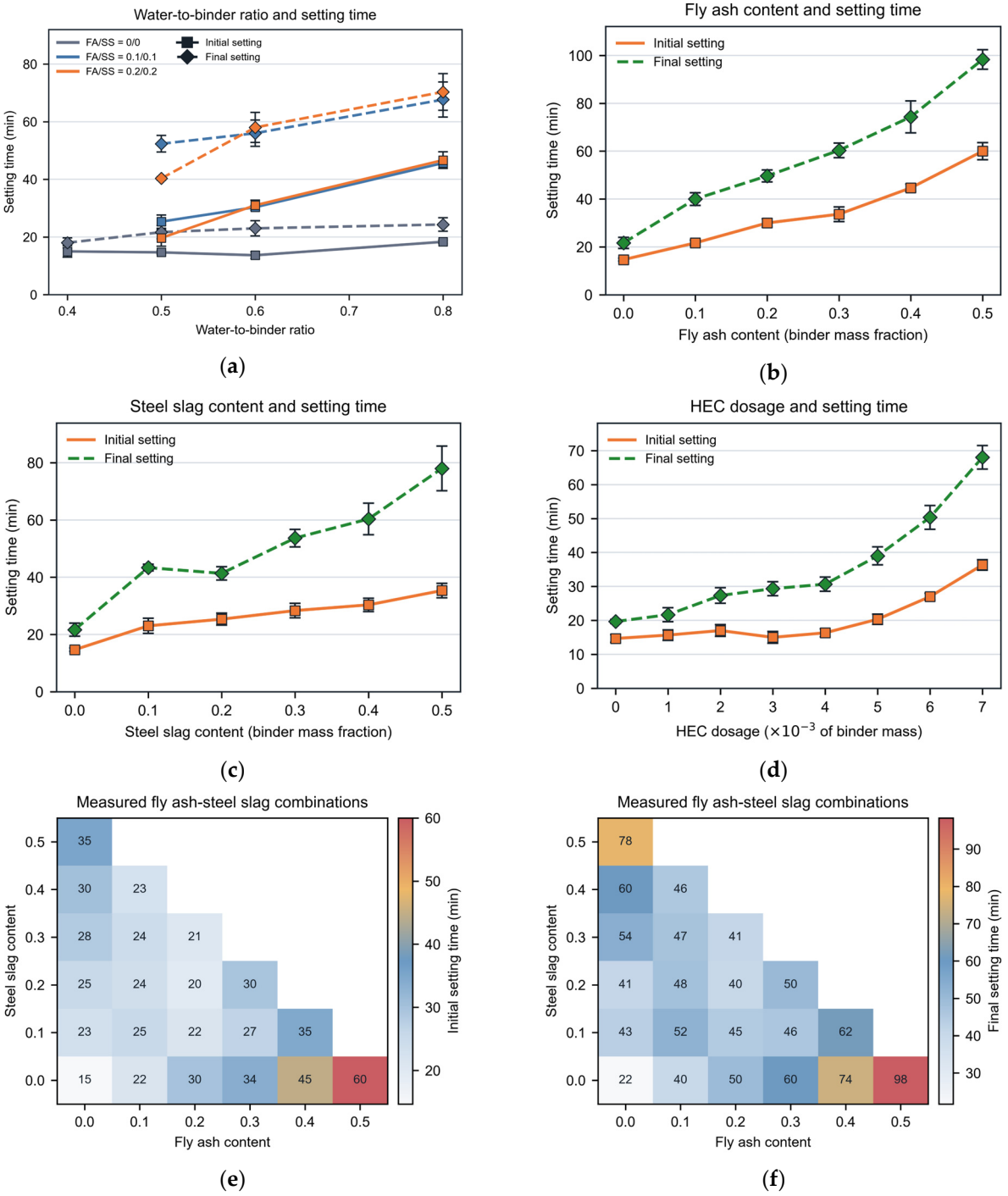


Figure 2. Effects of mixture variables on initial and final setting times: (**a**) water-to-binder ratio; (**b**) Class F fly ash content; (**c**) steel slag content; (**d**) HEC dosage; (**e**) initial-setting heat map; (**f**) final-setting heat map.

Fly ash produced the most pronounced retardation among the mineral additions (Figure 2b). Increasing the fly ash fraction from 0 to 0.50 extended the initial setting time

from 15 to 60 min and the final setting time from 22 to 98 min. For SAC pastes, setting is closely related to early ye'elimite hydration and the rapid formation of ettringite-bearing products. Replacing SAC with Class F fly ash reduces the proportion of rapidly reacting clinker phases and introduces a supplementary component with lower early reactivity. This can slow the accumulation and interconnection of early hydration products required to form a rigid skeleton, thereby extending both initial and final setting times [16,19]. However, the influence of fly ash depends on sulfate availability and binder composition. Ioannou et al. reported that fly ash shortened the final setting time in a calcium sulfoaluminate-calcium sulfate system containing anhydrite [16], indicating that this effect should not be generalized beyond the investigated mixture system.

Steel slag also generally prolonged setting but produced a less regular response (Figure 2c). Increasing the steel slag fraction from 0 to 0.50 extended the initial setting time from 15 to 35 min and the final setting time from 22 to 78 min. The final setting time decreased slightly from 43 min at a steel slag fraction of 0.10 to 41 min at 0.20, indicating a non-monotonic response at low replacement levels. This response may reflect the combined influence of SAC dilution, the lower early reactivity of steel slag, and the contribution of calcium-bearing phases in steel slag to the evolving hydration environment [44,48]. Therefore, the setting response of steel-slag-containing SAC paste should be interpreted as composition-dependent rather than as a simple replacement-level effect.

The HEC series was evaluated at a fixed water-to-binder ratio of 0.50 using a binder containing 80% SAC, 10% fly ash, and 10% steel slag. At HEC dosages up to 0.004, the initial setting time remained between 15 and 17 min, whereas the final setting time increased from 20 to 31 min (Figure 2d). At higher dosages, both setting times increased rapidly, reaching 36 and 68 min at an HEC dosage of 0.007. Since adsorption, pore-solution viscosity, polymer-network formation, and ion transport were not measured, HEC can modify setting through several coupled processes, including water sorption, adsorption on cement particles, increased pore-solution viscosity, and polymer-network formation, as reported in previous studies. These effects may restrict water and ion transport and can delay the contact and intergrowth of early hydration products, thereby postponing the formation of a continuous load-bearing skeleton [23,24]. Thus, HEC had a limited influence on initial setting at low dosages but caused pronounced retardation at higher dosages.

Figure 2e,f further show that setting time depended on the relative proportions of fly ash and steel slag rather than only on their total replacement. At a total replacement fraction of 0.40, the initial/final setting times were 45/74 min for 40% fly ash, 20/40 min for 20% fly ash—20% steel slag, and 30/60 min for 40% steel slag. The substantially shorter setting times of the blended mixture indicate that the effects of the two additions were not simply additive but depended on their relative proportions. This composition-dependent response is consistent with previous evidence that the influence of fly ash on SAC setting depends strongly on the binder composition and sulfate environment [16].

3.3. Compressive Strength

Figure 3 shows the effect of HEC dosage on the 7 and 28 d compressive strengths of the reference mixture with a water-to-binder ratio of 0.50 and a binder containing 80% SAC, 10% fly ash, and 10% steel slag. Both strengths decreased continuously with increasing HEC dosage. The 7 d compressive strength decreased from 31.3 MPa without HEC to 15.2 MPa at an HEC dosage of 0.007, corresponding to a reduction of 51.5%. Similarly, the 28 d strength decreased from 39.9 to 23.7 MPa, representing a reduction of 40.7%. Although the 28 d strength remained higher than the corresponding 7 d strength, later-age strength development did not compensate fully for the adverse effect of HEC.

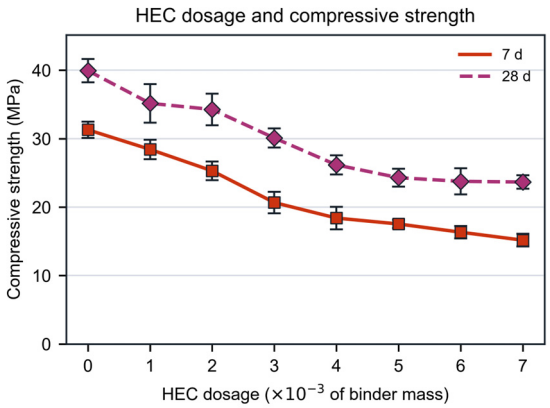
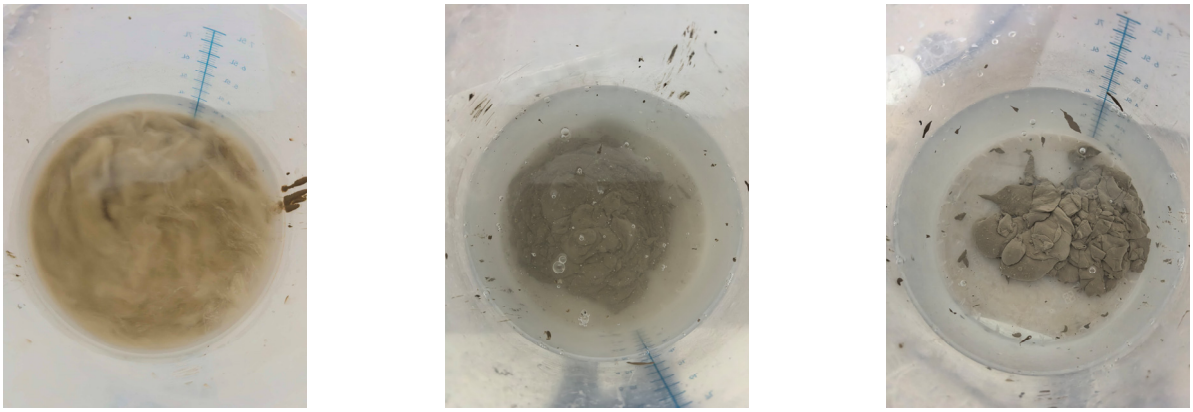


Figure 3. Effect of HEC dosage on the 7 and 28 d compressive strength.

Since air content, porosity, and hydration products were not measured, the strength reduction may be associated with increased air entrainment, higher porosity, and delayed early hydration as suggested by previous studies. Li et al. [49] reported that HEC reduced the mechanical strength of calcium sulfoaluminate cement mortar, although its effect was weaker than that of some other cellulose ethers. Hydroxyethyl methyl cellulose has also been reported to introduce micron-scale pores and increase the porosity of calcium sulfoaluminate cement mortar, thereby reducing compressive strength [50]. These findings are consistent with the present results.

3.4. Static-Water Dispersion Resistance

Figures 4 and 5 show the effects of the water-to-binder ratio and HEC dosage on the static-water turbidity of mixtures containing 80% SAC, 10% fly ash, and 10% steel slag. At an HEC dosage of 0.003, all readings exceeded the 400 NTU measurement limit and were treated as right-censored observations. At HEC dosages of 0.004 and 0.006, turbidity ranged from 180.3–250.2 NTU to 9.6–39.9 NTU, respectively. Increasing the HEC dosage from 0.004 to 0.006 reduced turbidity by 94.7%, 93.6%, and 84.1% at water-to-binder ratios of 0.40, 0.50, and 0.60, respectively.



(**a**) (**b**) (**c**)

Figure 4. Effect of HEC dosage on turbidity: (**a**) HEC dosage at a water-to-binder ratio of 0.40; (**b**) HEC dosage at a water-to-binder ratio of 0.50; (**c**) HEC dosage at a water-to-binder ratio of 0.60.

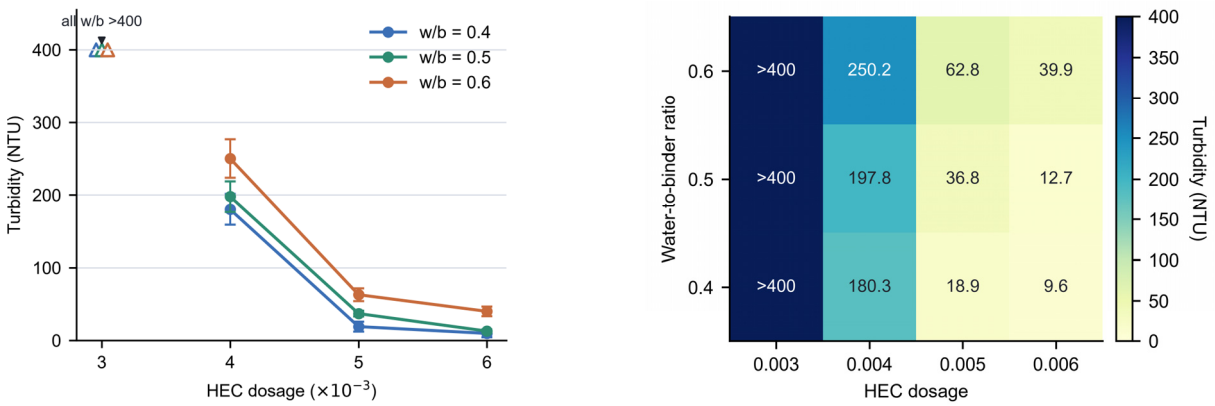


Figure 5. Effects of water-to-binder ratio and HEC dosage on static-water turbidity: (**a**) turbidity variation with HEC dosage; (**b**) response heatmap of turbidity across the investigated mixtures.

For the quantifiable data, both the water-to-binder ratio and HEC dosage significantly affected turbidity, whereas their interaction was not significant. Since viscosity and cohesion were not measured directly, the reduction in turbidity can be attributed to the viscosity-enhancing, water-retention, and cohesion-improving effects of HEC as reported in the literature. After hydration, HEC chains increase the viscosity of the liquid phase and may form a polymer network within the fresh paste, which may restrict water migration and reduce the release of fine cementitious particles into the surrounding water [21,25,26,51]. This mechanism is consistent with previous anti-washout grout studies in which turbidity was used as an indicator of particle dispersion into water [6,7]. The higher turbidity observed at larger water-to-binder ratios can be explained by the lower solid concentration and weaker cohesion of the paste, which make fine particles more susceptible to separation and suspension during water contact. However, turbidity reflects suspended-particle release rather than total material retention, flowing-water erosion, or underwater hardened performance. The results should therefore be interpreted as evidence of improved static-water dispersion resistance rather than complete anti-washout performance.

This improvement was accompanied by reduced workability and strength. In the companion HEC series with the same binder composition and a water-to-binder ratio of 0.50, an HEC dosage of 0.006 reduced flowability to 234.5 mm, while the 7 and 28 d compressive strengths were 16.3 and 23.8 MPa, respectively. HEC dosage should therefore be selected by balancing static-water dispersion resistance, flowability, setting time, and compressive strength.

4. Machine-Learning Methods and Results

4.1. Dataset Construction and Preprocessing

4.1.1. Dataset Description

The machine-learning dataset represented mixtures prepared using R-SAC 42.5 sulfoaluminate cement, Class F fly ash, 200-mesh steel slag powder, PCE, and tap water. Fly ash and steel slag partially replaced SAC and were expressed as mass fractions of the total binder.

The dataset comprised 31 HEC-free mixtures in which the water-to-binder ratio, fly ash content, steel slag content, and PCE dosage were varied. These four parameters were used as model inputs, while flowability and initial and final setting times were used as outputs. The HEC performance and static-water turbidity series were not included in model development. Flowability was calculated as the mean of three independently prepared flowability tests, while the setting times were calculated from three independently prepared

replicates. The unrounded mean values were retained for model training and evaluation. The statistical characteristics of the dataset are summarized in Table 2.

Table 2. Statistical data of the machine-learning dataset.

Type	Variable	Unit	Minimum	Maximum	Mean
Input	Water-to-binder ratio	-	0.4	0.8	0.535
Input	Fly ash content	-	0	0.5	0.152
Input	Steel slag content	-	0	0.5	0.152
Input	PCE dosage	mL	0	3.0	0.194
Output	Flowability	mm	253.5	336.5	288.3
Output	Initial setting time	min	14	60	28
Output	Final setting time	min	18	98	50

The water-to-binder ratio ranged from 0.40 to 0.80, the fly ash and steel slag fractions each ranged from 0 to 0.50, and the PCE dosage ranged from 0 to 3 mL. The measured flowability ranged from 253.5 to 336.5 mm, while the initial and final setting times ranged from 14 to 60 min and from 18 to 98 min, respectively.

4.1.2. Data Preprocessing and Nested Validation

Before model development, the dataset was checked for missing and invalid values, and the inputs and outputs were matched using the mixture identification numbers. No missing values were identified. Standardization was applied to the scale-sensitive models, including Ridge, SVR, KNN, and Kernel Ridge:

$$x_{std} = (x - \mu)/\sigma$$

where x_{std} is the standardized value, and μ and σ are the mean and standard deviation estimated from the corresponding training data. The SVR target values were also standardized during model fitting. All scaling parameters were estimated within the relevant training fold and applied subsequently to the validation or test data, thereby preventing data leakage. Tree-based models were trained using the original input scales.

Since the dataset contained only 31 mixtures, nested cross-validation was used for hyperparameter selection and performance evaluation. The validation procedure consisted of an outer leave-one-out cross-validation loop and an inner five-fold cross-validation loop. In each outer iteration, one mixture was held out as the test sample, while the remaining 30 mixtures formed the outer training set. Within this outer training set, five-fold cross-validation was used to select the hyperparameter combination that minimized the validation RMSE. The selected model was then refitted using all 30 outer-training mixtures and applied once to the held-out mixture. This procedure was repeated 31 times, so that each mixture was predicted once as an out-of-fold test sample. All preprocessing parameters, including standardization, were estimated only from the corresponding training fold and then applied to the validation or test sample.

4.2. Machine-Learning Models and Evaluation Methods

4.2.1. Selection of Machine-Learning Models

Seven regression algorithms were evaluated to establish relationships between the mixture variables and measured properties. The models were chosen to provide a deliberately broad but relatively simple candidate set suitable for a small experimental dataset. Ridge regression was included as a regularized linear baseline; KNN represented local similarity-

based prediction; SVR and Kernel Ridge represented kernel-based nonlinear regression; and Random Forest, Extra Trees, and Gradient Boosting represented tree-ensemble approaches capable of capturing nonlinear and interaction effects [52–58]. Thus, the selected methods covered different bias-variance trade-offs without relying on a single pre-assumed optimal algorithm.

Ridge regression was used as the linear baseline. It applies an L_2 penalty to reduce coefficient instability arising from correlations among input variables [52]. Support vector regression (SVR) with a radial basis function kernel was used to represent nonlinear relationships while controlling model complexity through the regularization parameter C and insensitive-loss parameter ε [53]. K-nearest-neighbour regression estimates an output from neighbouring observations in the feature space and was included as a local nonparametric method [54]. Kernel Ridge combines ridge regularization with a kernel transformation, enabling nonlinear regression in a transformed feature space [55].

Three tree-based ensemble models were also evaluated. Random Forest averages regression trees constructed using bootstrap samples and randomized feature selection to reduce prediction variance [56]. Extra Trees introduces additional randomness through randomly selected split thresholds, thereby increasing diversity among the individual trees [57]. Gradient Boosting sequentially constructs weak regression trees, with each new tree fitted to reduce the residual errors of the preceding ensemble [58].

The hyperparameter search spaces are summarized in Table 3. Within each outer LOOCV training set, hyperparameters were selected separately for each model and predicted property by minimizing the mean inner-validation RMSE. The same predefined search spaces were used in every outer iteration. Logarithmically spaced values were considered for regularization and kernel parameters, while restricted ranges were used for tree depth and neighbourhood size to limit model complexity given the small dataset. Scale-sensitive models were fitted using the standardization procedure described in Section 4.1.2, whereas tree-based models used the original input scales. A random seed of 42 was used for the stochastic ensemble models to ensure reproducibility.

Table 3. Hyperparameter search space.

Model	Hyperparameter Search Space
Ridge	α: 0.01, 0.1, 1, 10, 100
SVR	C: 1, 10, 100; γ: scale, 0.1, 1; ε: 0.01, 0.1, 0.2
KNN	k: 2, 3, 5, 7; weights: uniform/distance; p: 1, 2
Kernel Ridge	α: 0.01, 0.1, 1, 10; γ: 0.01, 0.1, 0.5, 1
Random Forest	Trees: 300; depth: 2, 4, None; leaf: 1, 2; features: 1.0, sqrt
Extra Trees	Trees: 300; depth: 2, 4, None; leaf: 1, 2; features: 1.0, sqrt
Gradient Boosting	Estimators: 50, 150; rate: 0.03, 0.1; depth: 1, 2; leaf: 1, 2

4.2.2. Model Evaluation

The predictive performance of each potential algorithm was evaluated using the outer-loop predictions generated by nested cross-validation. In each outer LOOCV iteration, hyperparameters for each potential model were selected exclusively within the 30-sample training set using five-fold cross-validation. The selected configuration was then refitted using the complete outer training set and applied to the held-out mixture. Thus, the outer test sample was not involved in standardization, hyperparameter selection, or model fitting. This procedure avoided the optimistic bias that can arise when the same resampling results are used for both model selection and performance evaluation [34].

After completing all 31 outer iterations, the pooled out-of-fold predictions were evaluated using the coefficient of determination (R^2), root-mean-square error (RMSE), and mean absolute error (MAE):

$$R^2 = 1 - \frac{\sum_{i=1}^{n}(y_i - \hat{y}_i)^2}{\sum_{i=1}^{n}(y_i - \overline{y})^2}$$

$$\text{RMSE} = \sqrt{\frac{1}{n}\sum_{i=1}^{n}(y_i - \hat{y}_i)^2}$$

$$\text{MAE} = \frac{1}{n}\sum_{i=1}^{n}|y_i - \hat{y}_i|$$

where y_i and $\hat{y}_i$ are the measured and predicted values, respectively; $\overline{y}$ is the mean measured value; and n is the number of samples. A higher R^2 indicates better agreement between the measured and predicted values, whereas lower RMSE and MAE values indicate smaller prediction errors. RMSE gives greater weight to large deviations, while MAE represents the average absolute prediction error. The models were compared separately for flowability, initial setting time, and final setting time. For each output property, the model with the lowest observed outer-loop RMSE was identified as the apparent best-performing model; MAE was used as the secondary criterion when necessary. The complete comparison results are presented in Table 4.

Table 4. Nested-LOOCV performance of the potential models.

Predicted Property	Model	R^2	RMSE	MAE
Flowability (mm)	Ridge	0.774	11.608	9.266
	SVR	0.785	11.318	9.144
	KNN	0.673	13.950	9.081
	Kernel Ridge	0.627	14.912	11.056
	Random Forest	0.679	13.819	10.866
	Extra Trees	0.819	10.397	7.808
	Gradient Boosting	0.752	12.148	9.659
Initial setting time (min.)	Ridge	0.247	8.762	7.100
	SVR	0.743	5.122	3.706
	KNN	0.368	8.028	5.226
	Kernel Ridge	0.622	6.208	4.129
	Random Forest	0.542	6.833	4.997
	Extra Trees	0.718	5.366	3.649
	Gradient Boosting	0.481	7.274	5.256
Final setting time (min.)	Ridge	0.270	14.245	11.554
	SVR	0.676	9.494	6.958
	KNN	0.457	12.279	8.593
	Kernel Ridge	0.600	10.547	7.284
	Random Forest	0.603	10.510	8.132
	Extra Trees	0.767	8.041	5.851
	Gradient Boosting	0.595	10.607	8.279

4.2.3. SHAP-Based Model Interpretation

SHAP was used to quantify the contribution of each input variable to the selected model predictions [35]. For each outer LOOCV iteration, exact model-agnostic SHAP values were calculated for the held-out mixture using only the fitted outer-training model. An Independent masker constructed from the 30 outer-training mixtures was used as the background distribution, and the held-out mixture was not included in either model fitting or background construction. Global importance was calculated as the mean absolute out-of-fold SHAP value across all 31 mixtures. To assess ranking stability, the mixture-level out-of-fold SHAP values were resampled 10,000 times with replacement using a fixed random seed. Bootstrap percentile 95% intervals and the probability of each variable being ranked first were then calculated. SHAP values were interpreted as model-based attributions rather than causal effects, particularly because the mixture variables were compositionally constrained.

4.3. Prediction Performance and Model Interpretation

4.3.1. Prediction Performance

Table 5 summarizes the best-performing model for each target property, while Figure 6 compares the corresponding nested-LOOCV predictions with the measured results. Extra Trees was selected for flowability, SVR for initial setting time, and Extra Trees for final setting time. These output-specific results identify the algorithms that performed best under the present validation procedure, but the selected model types do not establish whether the underlying material responses are linear or governed by specific physical interactions. Similar output-dependent differences in model performance have been reported in data-driven concrete studies [28,33,59].

Table 5. Models with the lowest observed outer-loop RMSE for each predicted property.

Predicted Property	Model with Lowest Observed RMSE	R^2	RMSE	MAE
Flowability	Extra Trees	0.819	10.397 mm	7.808 mm
Initial setting time	SVR	0.743	5.122 min	3.706 min
Final setting time	Extra Trees	0.767	8.041 min	5.851 min

As shown in Figure 6a, Extra Trees provided the best flowability prediction, with an R^2 of 0.819, an RMSE of 10.397 mm, and an MAE of 7.808 mm. Most predictions followed the measured trend, although several mixtures in the upper flowability range were underestimated. The selected model represents the best predictive result under the specified nested-validation procedure and should not be interpreted as direct evidence of a particular physical mechanism or functional relationship.

For initial setting time, SVR achieved an R^2 of 0.743, an RMSE of 5.122 min, and an MAE of 3.706 min (Figure 6b). The model reproduced the overall variation in initial setting time, although deviations remained near the boundaries of the measured range. The relatively similar performance of SVR and Extra Trees shown in Table 4 also indicates that the selected algorithm should not be regarded as uniquely superior for this limited dataset.

For final setting time, Extra Trees achieved an R^2 of 0.767, an RMSE of 8.041 min, and an MAE of 5.851 min (Figure 6c). Most intermediate observations were represented reasonably well, whereas the longest setting times remained underestimated. The contributions of the individual mixture variables were therefore evaluated separately using out-of-fold SHAP values rather than inferred from the selected model type.

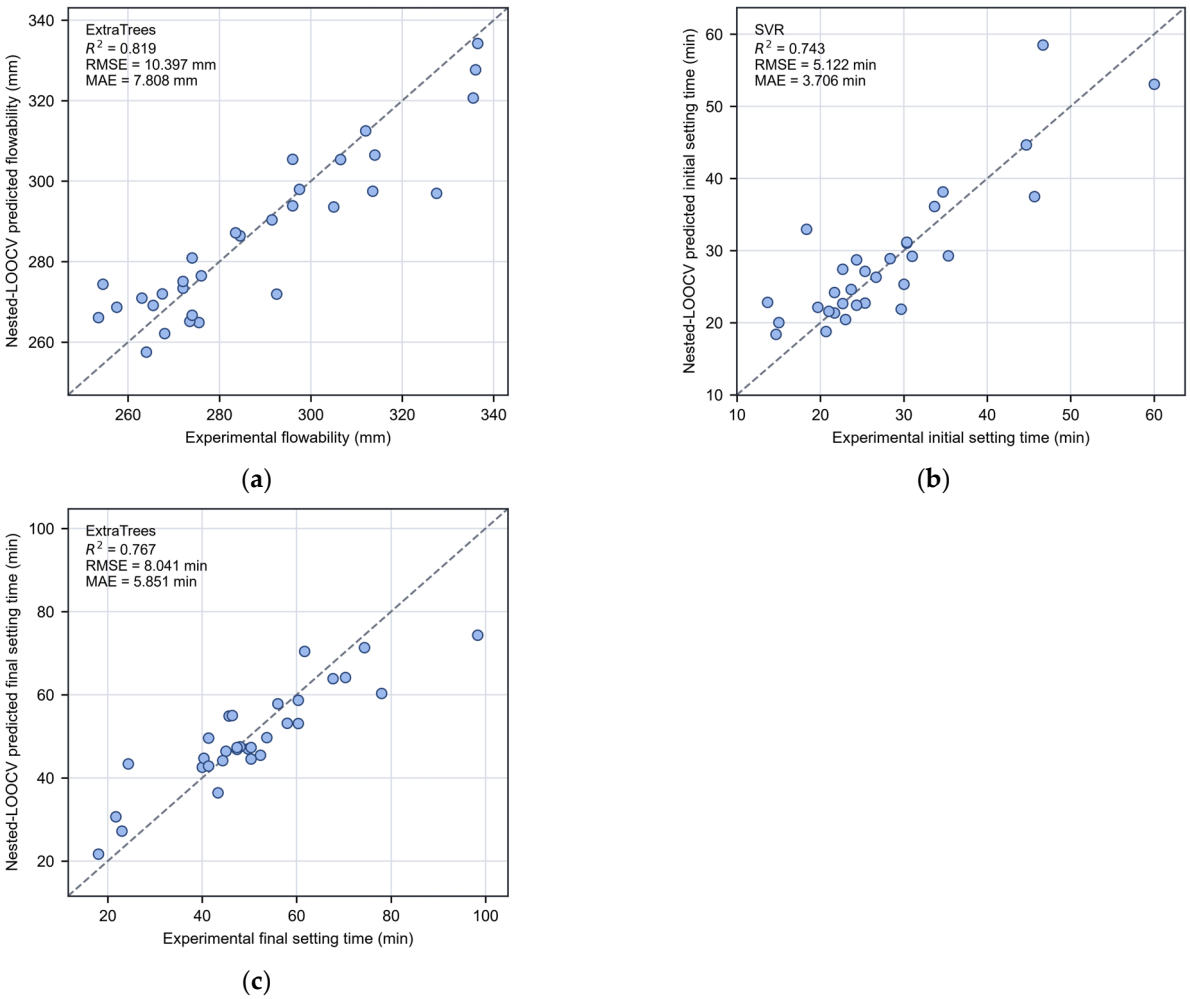


Figure 6. Measured and nested-LOOCV-predicted values: (**a**) flowability predicted using Extra Trees; (**b**) initial setting time predicted using SVR; (**c**) final setting time predicted using Extra Trees.

The predictive accuracy obtained in this study was lower than that reported in some previous mortar and concrete studies. Baah et al. obtained an R^2 of 0.957 for predicting 28 d mortar strength using 113 samples and an XGBoost model [33], whereas Zheng et al. reported R^2 values above 0.97 after hyperparameter optimization and feature selection using 610 concrete mixtures [53]. These results are not directly comparable because the predicted properties, dataset sizes, input variables, validation strategies, and model-tuning procedures differed substantially. Reviews of concrete-property prediction have similarly emphasized that model performance depends strongly on dataset size, data quality, input selection, and the investigated material system [27]. Therefore, the results show that the selected mixture parameters can provide preliminary predictions of flowability and setting time.

4.3.2. SHAP-Based Interpretation of Mixture Variables

Figure 7 presents the out-of-fold SHAP distributions, while Table 6 summarizes the corresponding mean absolute SHAP values. For the Extra Trees flowability model, the water-to-binder ratio was the dominant input, with a mean absolute SHAP value of 13.805 mm. Higher water-to-binder ratios produced strongly positive SHAP values, whereas lower ratios generally produced negative contributions. Fly ash and steel slag had smaller mean absolute SHAP values of 6.040 and 5.453 mm, respectively. Higher fly ash fractions generally increased predicted flowability, while high steel slag fractions tended to produce

negative contributions. These model-based patterns were broadly consistent with the controlled experimental results in Section 3.1. The water-to-binder ratio was ranked first in 99.99% of the bootstrap resamples, indicating that its dominant contribution was stable within the present dataset.

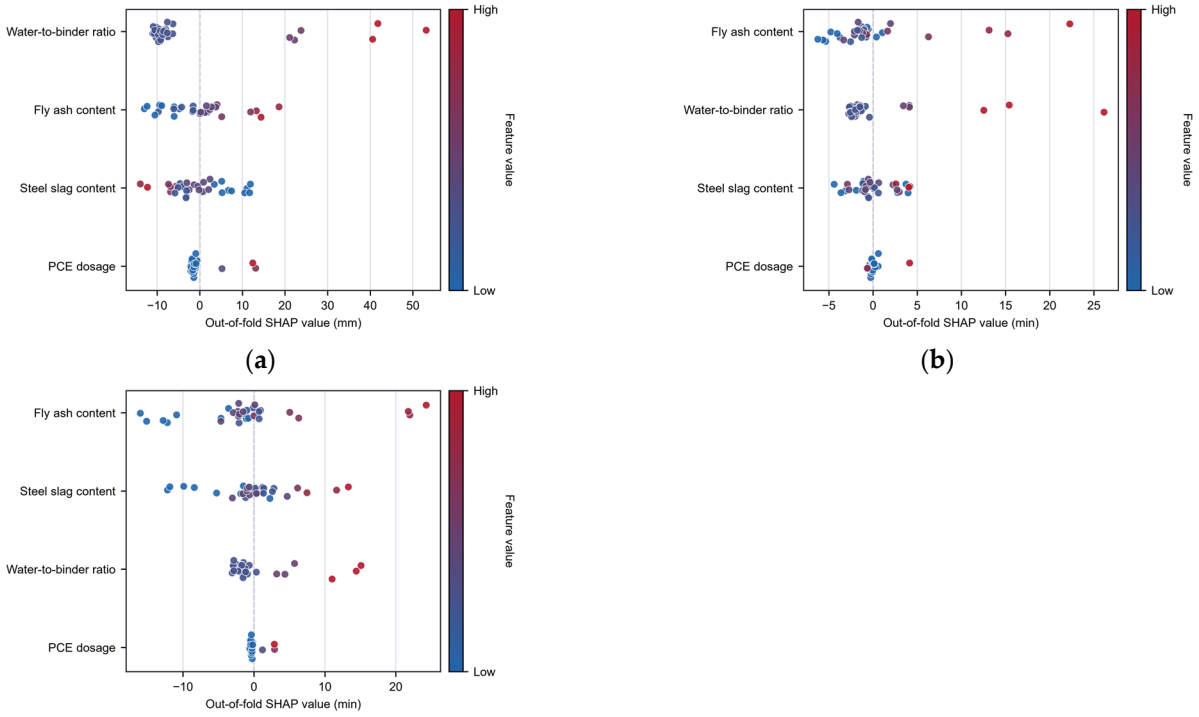


Figure 7. Out-of-fold SHAP distributions for the selected models: (**a**) flowability predicted using Extra Trees; (**b**) initial setting time predicted using SVR; (**c**) final setting time predicted using Extra Trees.

Table 6. Mean absolute out-of-fold SHAP values for the selected prediction models.

Input Variable	Flowability (mm)	Initial Setting Time (min)	Final Setting Time (min)
Water-to-binder ratio	13.805	3.701	3.258
Fly ash content	6.04	3.787	5.902
Steel slag content	5.453	1.867	3.782

For initial setting time, fly ash and the water-to-binder ratio had similar mean absolute SHAP values of 3.787 and 3.701 min, respectively, followed by steel slag at 1.867 min. Higher fly ash fractions were generally associated with positive SHAP values and therefore longer predicted initial setting times. However, fly ash and the water-to-binder ratio were ranked first in 52.81% and 47.19% of the bootstrap resamples, respectively, indicating that their relative ranking was not stable. For final setting time, fly ash was the most influential input, with a mean absolute SHAP value of 5.902 min, followed by steel slag at 3.782 min and the water-to-binder ratio at 3.258 min. Fly ash was ranked first in 92.32% of the bootstrap resamples, indicating a comparatively stable dominant contribution. The positive contributions associated with high fly ash and steel slag fractions were consistent with the experimentally observed setting retardation described in Section 3.2.

4.3.3. Mixture-Property Prediction and Staged Formulation Assessment

To obtain formulation-level predictions, the selected Extra Trees, SVR, and Extra Trees models for flowability, initial setting time, and final setting time, respectively, were refitted

using all 31 observations. Prediction uncertainty was quantified using Jackknife+ [36]. For each target property, 31 leave-one-out models were fitted, and potential predictions were combined with the corresponding absolute residuals to construct nominal 80%, 90%, and 95% prediction intervals. Unlike global cross-validation metrics, these intervals describe the uncertainty associated with an individual formulation-level prediction [60].

Figure 8 presents a reconstruction of the reference formulation used in the HEC performance series, with a water-to-binder ratio of 0.50, fly ash and steel slag fractions of 0.10, and no PCE. The predicted flowability, initial setting time, and final setting time were 254.5 mm, 23 min, and 52 min, respectively. The corresponding nominal 90% Jackknife+ prediction intervals were 224.0–294.3 mm, 9–38 min, and 28–76 min, respectively. Owing to the limited number of leave-one-out fits, the nominal 90% and 95% intervals corresponded to the same finite-sample order statistics and therefore coincided. The wider relative intervals for the setting-time predictions indicate greater uncertainty than that associated with flowability.

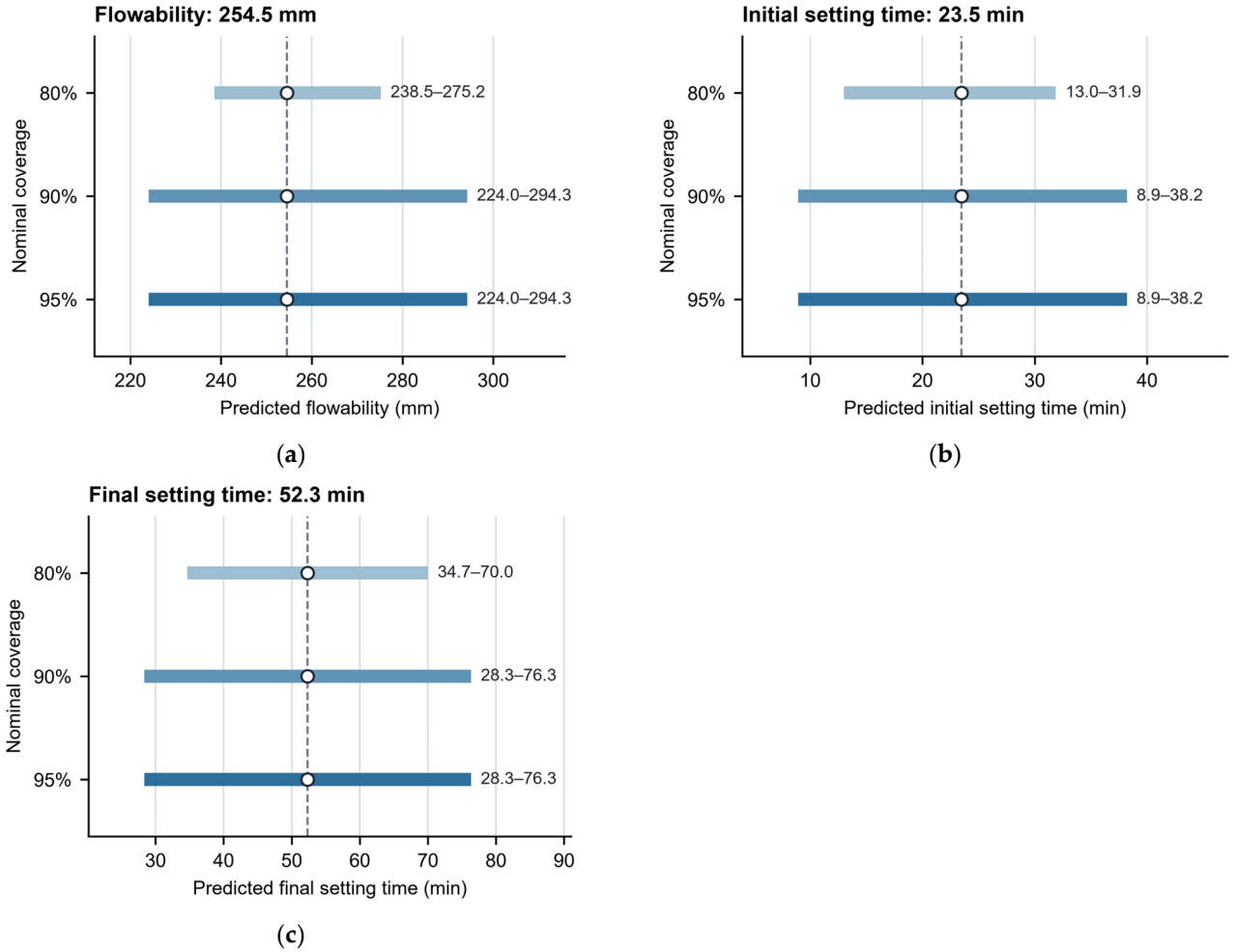


Figure 8. Point predictions and nominal Jackknife+ prediction intervals for the reference formulation: (**a**) flowability; (**b**) initial setting time; (**c**) final setting time.

The models therefore provide a preliminary screening tool for HEC-free base formulations within the investigated composition domain. Point predictions allow formulations to be compared and ranked according to flowability and setting time, while prediction intervals communicate the uncertainty of each estimate. The experimental HEC series complements this model-based screening by evaluating the effects of HEC on workabil-

ity, setting behaviour, compressive strength, and static-water dispersion resistance of the reference binder.

5. Conclusions

This study shows that SAC-based grout for water-rich tunnel applications should be designed by balancing rapid setting, sufficient workability, static-water dispersion resistance, and mechanical strength, rather than by optimizing any single property. The following conclusions were drawn:

1. The water-to-binder ratio, fly ash, steel slag, PCE, and HEC jointly controlled the fresh-state behaviour of the grout. Higher water-to-binder ratio, fly ash content, and PCE dosage generally improved flowability, whereas excessive HEC reduced flowability. Fly ash and steel slag generally prolonged setting, but their combined effects were composition-dependent, indicating that binder replacement should be selected according to the targeted workability-setting window.
2. HEC was the most effective variable for improving static-water dispersion resistance. Increasing the HEC dosage from 0.004 to 0.006 reduced turbidity by 84.1–94.7%, but this benefit was accompanied by reduced flowability and compressive strength. Therefore, HEC dosage should be treated as a trade-off parameter: sufficient to suppress particle dispersion, but limited to avoid unacceptable losses in pumpability and hardened performance.
3. The machine-learning models provided useful preliminary predictions of flowability and setting time within the investigated HEC-free dataset. Extra Trees, SVR, and Extra Trees gave the lowest observed outer-loop errors for flowability, initial setting time, and final setting time, respectively, with R^2 values of 0.819, 0.743, and 0.767. SHAP analysis indicated that the water-to-binder ratio was the dominant input for flowability prediction, while fly ash was a key input for setting-time prediction.
4. The practical role of the machine-learning component is preliminary comparison of HEC-free base formulations, not final engineering qualification. Future work should expand the dataset to include HEC-modified mixtures, compressive strength, and dispersion-related outputs, and should validate selected formulations using independent material batches and dynamic-water washout tests before field application.

Author Contributions: T.P.: Conceptualization, methodology, data curation, writing—original draft preparation; D.R.: investigation, writing—original draft preparation; B.L.: writing—original draft preparation; H.L.: writing—review and editing; P.X.: writing—review and editing and Y.L.: Conceptualization, writing—review and editing. All authors have read and agreed to the published version of the manuscript.

Funding: This research was funded by China MCC5 Group Key Research and Development Special Program (WY2024B001).

Data Availability Statement: The data presented in this study are available from the corresponding author upon reasonable request.

Conflicts of Interest: Author T.P., B.L. and H.L. were employed by the company China MCC5 Group Corp. Ltd. Author T.P., D.R., B.L., P.X. and H.L. were employed by the company Chengdu Surveying Geotechnical Research Institute Co., Ltd. of MCC. The remaining author declare that the research was conducted in the absence of any commercial or financial relationships that could be construed as a potential conflict of interest.

Appendix A

The test matrix and data are available via the following link: https://docs.qq.com/sheet/DV01OSnNzdGdVdGNm?tab=BB08J2 (assessed on 1 September 2026).

References

1. Qian, Q.; Lin, P. Safety risk management of underground engineering in China: Progress, challenges and strategies. *J. Rock Mech. Geotech. Eng.* **2016**, *8*, 423–442. [CrossRef]
2. Zhao, Y.; Li, P.; Tian, S. Prevention and treatment technologies of railway tunnel water inrush and mud gushing in China. *J. Rock Mech. Geotech. Eng.* **2013**, *5*, 468–477. [CrossRef]
3. Li, S.; Liu, R.; Zhang, Q.; Zhang, X. Protection against water or mud inrush in tunnels by grouting: A review. *J. Rock Mech. Geotech. Eng.* **2016**, *8*, 753–766. [CrossRef]
4. Zhang, C.; Fu, J.; Yang, J.; Ou, X.; Ye, X.; Zhang, Y. Formulation and performance of grouting materials for underwater shield tunnel construction in karst ground. *Constr. Build. Mater.* **2018**, *187*, 327–338. [CrossRef]
5. Li, S.; Zhang, J.; Li, Z.; Gao, Y.; Qi, Y.; Li, H.; Zhang, Q. Investigation and practical application of a new cementitious anti-washout grouting material. *Constr. Build. Mater.* **2019**, *224*, 66–77. [CrossRef]
6. Lu, H.; Sun, X.; Ma, H. Anti-washout concrete: An overview. *Constr. Build. Mater.* **2022**, *344*, 128151. [CrossRef]
7. Khayat, K.H.; Yahia, A. Simple field tests to characterize fluidity and washout resistance of structural cement grout. *Cem. Concr. Aggreg.* **1998**, *20*, 145–156. [CrossRef]
8. Yahia, A.; Khayat, K.H. Experiment design to evaluate interaction of high-range water-reducer and anti-washout admixture in high-performance cement grout. *Cem. Concr. Res.* **2001**, *31*, 749–757. [CrossRef]
9. Cui, W.; Huang, J.; Song, H.; Xiao, M. Development of two new anti-washout grouting materials using multi-way ANOVA in conjunction with grey relational analysis. *Constr. Build. Mater.* **2017**, *156*, 184–198. [CrossRef]
10. Guo, H.; Tang, Z.; Liu, Q.; Xu, J.; Wang, M.; Liang, R.; Sun, G. Ultra-stable anti-washout cement grout achieved by super water absorbing villus-like nanocomposite hydrogel. *Constr. Build. Mater.* **2021**, *301*, 124035. [CrossRef]
11. Sun, Z.; Li, Y.; Ming, X.; Chen, B.; Li, Z. Enhancing anti-washout behavior of cement paste by polyacrylamide gelation: From floc properties to mechanism. *Cem. Concr. Compos.* **2023**, *136*, 104887. [CrossRef]
12. Bessaies-Bey, H.; Khayat, K.H.; Palacios, M.; Schmidt, W.; Roussel, N. Viscosity modifying agents: Key components of advanced cement-based materials with adapted rheology. *Cem. Concr. Res.* **2022**, *152*, 106646. [CrossRef]
13. Glasser, F.P.; Zhang, L. High-performance cement matrices based on calcium sulfoaluminate-belite compositions. *Cem. Concr. Res.* **2001**, *31*, 1881–1886. [CrossRef]
14. Gartner, E. Industrially interesting approaches to low-CO2 cements. *Cem. Concr. Res.* **2004**, *34*, 1489–1498. [CrossRef]
15. Winnefeld, F.; Lothenbach, B. Hydration of calcium sulfoaluminate cements: Experimental findings and thermodynamic modelling. *Cem. Concr. Res.* **2010**, *40*, 1239–1247. [CrossRef]
16. Ioannou, S.; Reig, L.; Paine, K.; Quillin, K. Properties of a ternary calcium sulfoaluminate-calcium sulfate-fly ash cement. *Cem. Concr. Res.* **2014**, *56*, 75–83. [CrossRef]
17. Sha, F.; Fan, R.; Gu, S.; Xi, M. Strengthening effect of sulphoaluminate cementitious grouting material for water-bearing broken rocky stratum. *Constr. Build. Mater.* **2023**, *368*, 130390. [CrossRef]
18. Sha, F.; Li, H.; Liu, P. Experimental study on sulfoaluminate cement-based grout. *Ceramics-Silikaty* **2020**, *64*, 249–262. [CrossRef]
19. Sha, F.; Li, S.; Liu, R.; Li, Z.; Zhang, Q. Experimental study on performance of cement-based grouts admixed with fly ash, bentonite, superplasticizer and water glass. *Constr. Build. Mater.* **2018**, *161*, 282–291. [CrossRef]
20. Sha, F.; Li, H.; Pan, D. Development of steel slag composite grouts for underground engineering. *J. Mater. Res. Technol.* **2020**, *9*, 2793–2809. [CrossRef]
21. Patural, L.; Marchal, P.; Govin, A.; Grosseau, P.; Ruot, B.; Devès, O. Cellulose ethers influence on water retention and consistency in cement-based mortars. *Cem. Concr. Res.* **2011**, *41*, 46–55. [CrossRef]
22. Pourchez, J.; Peschard, A.; Grosseau, P.; Guyonnet, R.; Guilhot, B.; Vallée, F. HPMC and HEMC influence on cement hydration. *Cem. Concr. Res.* **2006**, *36*, 288–294. [CrossRef]
23. Wan, Q.; Wang, Z.; Huang, T.; Wang, R. Water retention mechanism of cellulose ethers in calcium sulfoaluminate cement-based materials. *Constr. Build. Mater.* **2021**, *301*, 124118. [CrossRef]
24. Li, J.; Wang, R.; Xu, Y. Influence of cellulose ethers chemistry and substitution degree on the setting and early-stage hydration of calcium sulphoaluminate cement. *Constr. Build. Mater.* **2022**, *344*, 128266. [CrossRef]
25. Saric-Coric, M.; Khayat, K.H.; Tagnit-Hamou, A. Performance characteristics of cement grouts made with various combinations of high-range water reducer and cellulose-based viscosity modifier. *Cem. Concr. Res.* **2003**, *33*, 1999–2008. [CrossRef]
26. Plank, J.; Hirsch, C. Impact of zeta potential of early cement hydration phases on superplasticizer adsorption. *Cem. Concr. Res.* **2007**, *37*, 537–542. [CrossRef]
27. Vasconcellos, A.T.; Matos, P.R.; Casagrande, C.A.; Ribeiro, A.V.S.; Prudencio, L.R., Jr. Evaluating the variability of the modulus of elasticity of concrete through the use of different types and batches of aggregate. *Materia* **2021**, *26*, e13117. [CrossRef]
28. Ben Chaabene, W.; Flah, M.; Nehdi, M.L. Machine learning prediction of mechanical properties of concrete: Critical review. *Constr. Build. Mater.* **2020**, *260*, 119889. [CrossRef]

29. Liu, X.; Wang, S.; Liu, B.; Liu, Q.; Zhou, Y.; Chen, J.; Luo, J. Cement-based grouting material development and prediction of material properties using PSO-RBF machine learning. *Constr. Build. Mater.* **2024**, *417*, 135328. [CrossRef]
30. Ren, J.; Zhao, H.; Zhang, L.; Zhao, Z.; Xu, Y.; Cheng, Y.; Wang, M.; Chen, J.; Wang, J. Design optimization of cement grouting material based on adaptive boosting algorithm and simplicial homology global optimization. *J. Build. Eng.* **2022**, *49*, 104049. [CrossRef]
31. Zhang, C.; Yang, J.; Fu, J.; Wang, S.; Yin, J.; Ou, X.F.; Xie, Y. Optimal formulation design of polymer-modified cement-based grouting material for loose deposits. *Constr. Build. Mater.* **2020**, *261*, 120513. [CrossRef]
32. Zhang, J.; Huang, Y.; Wang, Y.; Ma, G. Multi-objective optimization of concrete mixture proportions using machine learning and metaheuristic algorithms. *Constr. Build. Mater.* **2020**, *253*, 119208. [CrossRef]
33. Baah, T.T.; Zeng, H.; Latypov, M.I.; Kim, H.J. Design of sustainable mortar incorporating construction and demolition waste through adaptive experiments accelerated by machine learning. *Results Eng.* **2025**, *25*, 104264. [CrossRef]
34. Varma, S.; Simon, R. Bias in error estimation when using cross-validation for model selection. *BMC Bioinform.* **2006**, *7*, 91. [CrossRef] [PubMed]
35. Lundberg, S.M.; Lee, S.-I. A unified approach to interpreting model predictions. In Proceedings of the 31st Conference on Neural Information Processing Systems (NIPS 2017), Long Beach, CA, USA, 4–9 December 2017; pp. 4765–4774.
36. Barber, R.F.; Candes, E.J.; Ramdas, A.; Tibshirani, R.J. Predictive inference with the Jackknife+. *Ann. Stat.* **2021**, *49*, 486–507. [CrossRef]
37. *GB/T 50448-2015*; Technical Code for Application of Cementitious Grout. China Architecture & Building Press: Beijing, China, 2015.
38. *GB/T 1346-2024*; Test Methods for Water Requirement of Standard Consistency, Setting Time and Soundness of the Portland Cement. Standards Press of China: Beijing, China, 2024.
39. *GB/T 17671-2021*; Test Method of Cement Mortar Strength (ISO Method). Standards Press of China: Beijing, China, 2021.
40. Nikvar-Hassani, A.; Manjarrez, L.; Zhang, L. Rheology, setting time, and compressive strength of Class F fly ash-based geopolymer binder containing ordinary Portland cement. *J. Mater. Civ. Eng.* **2022**, *34*, 04021409. [CrossRef]
41. Mondal, S.K.; Welz, A.; Clinton, C.; Khayat, K.H.; Kumar, A.; Okoronkwo, M.U. Quantifying the workability of calcium sulfoaluminate cement paste using time-dependent rheology. *Materials* **2022**, *15*, 5775. [CrossRef] [PubMed]
42. Du, H.; Zhao, Q.; Shi, X. High-volume fly ash-based cementitious composites as sustainable materials: An overview of recent advances. *Adv. Civ. Eng.* **2021**, *2021*, 4976169. [CrossRef]
43. Ioannou, S.; Paine, K.; Quillin, K. Influence of fly ash on the hydration of calcium sulfoaluminate cement. *Cem. Concr. Res.* **2017**, *95*, 152–163. [CrossRef]
44. Liao, Y.; Hu, M.; Yao, J.; Wang, K.; Tang, S.; Zuo, Y. Calcium sulfoaluminate cementitious materials with steel slag and calcined phosphogypsum: Hydration and physico-mechanical properties. *Constr. Build. Mater.* **2025**, *460*, 139795. [CrossRef]
45. Ke, G.; Zhang, J. Effects of retarding admixture, superplasticizer and supplementary cementitious material on the rheology and mechanical properties of high strength calcium sulfoaluminate cement paste. *J. Adv. Concr. Technol.* **2020**, *18*, 17–26. [CrossRef]
46. Wu, Y.; Li, Q.; Li, G.; Tang, S.; Niu, M.; Wu, Y. Effect of naphthalene-based superplasticizer and polycarboxylic acid superplasticizer on the properties of sulfoaluminate cement. *Materials* **2021**, *14*, 662. [CrossRef] [PubMed]
47. Wang, C.; Song, M. Influence of water-cement ratio and type of mixing water on the early hydration performance of calcium sulphoaluminate cement. *Adv. Mater. Sci. Eng.* **2021**, *2021*, 5557763. [CrossRef]
48. Liu, H.; Liu, C.; Wu, J.; Gao, Y.; Shao, J.; Wang, C.; Su, T.; Cao, F.; Zhang, W.; Yang, Q.; et al. Preparation of high-belite calcium sulfoaluminate cement and calcium sulfoaluminate cement from industrial solid waste: A review. *Sustainability* **2025**, *17*, 4269. [CrossRef]
49. Li, J.; Wang, R.; Li, L. Influence of cellulose ethers structure on mechanical strength of calcium sulphoaluminate cement mortar. *Constr. Build. Mater.* **2021**, *303*, 124514. [CrossRef]
50. Zhang, S.; Wang, R.; Xu, L.; Hecker, A.; Ludwig, H.-M.; Wang, P. Properties of calcium sulfoaluminate cement mortar modified by hydroxyethyl methyl celluloses with different degrees of substitution. *Molecules* **2021**, *26*, 2136. [CrossRef] [PubMed]
51. Murakami, K.; Satoh, A.; Konishi, H. Experimental study on mix proportion design of anti-washout grout with cellulose ether mixed. *AIJ J. Technol. Des.* **2023**, *29*, 1209–1214. [CrossRef]
52. Hoerl, A.E.; Kennard, R.W. Ridge regression: Biased estimation for nonorthogonal problems. *Technometrics* **1970**, *12*, 55–67. [CrossRef]
53. Drucker, H.; Burges, C.J.C.; Kaufman, L.; Smola, A.J.; Vapnik, V. Support vector regression machines. *Adv. Neural Inf. Process. Syst.* **1997**, *9*, 155–161.
54. Altman, N.S. An introduction to kernel and nearest-neighbor nonparametric regression. *Am. Stat.* **1992**, *46*, 175–185. [CrossRef]
55. Saunders, C.; Gammerman, A.; Vovk, V. Ridge regression learning algorithm in dual variables. In Proceedings of the 15th International Conference on Machine Learning, San Francisco, CA, USA, 24–27 July 1998; pp. 515–521.
56. Breiman, L. Random forests. *Mach. Learn.* **2001**, *45*, 5–32. [CrossRef]

57. Geurts, P.; Ernst, D.; Wehenkel, L. Extremely randomized trees. *Mach. Learn.* **2006**, *63*, 3–42. [CrossRef]
58. Friedman, J.H. Greedy function approximation: A gradient boosting machine. *Ann. Stat.* **2001**, *29*, 1189–1232. [CrossRef]
59. Zheng, W.; Shui, Z.; Xu, Z.; Gao, X.; Zhang, S. Multi-objective optimization of concrete mix design based on machine learning. *J. Build. Eng.* **2023**, *76*, 107396. [CrossRef]
60. Tavazza, F.; DeCost, B.; Choudhary, K. Uncertainty prediction for machine learning models of material properties. *ACS Omega* **2021**, *6*, 32431–32440. [CrossRef] [PubMed]

Disclaimer/Publisher's Note: The statements, opinions and data contained in all publications are solely those of the individual author(s) and contributor(s) and not of MDPI and/or the editor(s). MDPI and/or the editor(s) disclaim responsibility for any injury to people or property resulting from any ideas, methods, instructions or products referred to in the content.